SPATIALLY-RESOLVED HPGE GAMMA-RAY SPECTROSCOPY

FOR NUCLEAR FORENSICS

A Thesis

by

TIMOTHY WYKEHAM JACOMB-HOOD

Submitted to the Office of Graduate and Professional Studies of
Texas A&M University
in partial fulfillment of the requirements for the degree of

MASTER OF SCIENCE

Chair of Committee,	Craig Marianno
Committee Members,	Marvin Adams
	Sunil Chirayath
	Sunil Khatri
Head of Department,	Michael Nastasi

December 2020

Major Subject: Nuclear Engineering

ABSTRACT

The Germanium Gamma-ray Imager (GeGI) is a planar high purity germanium (HPGe) imaging detector developed by PHDS Co for far-field imaging. This research investigates the GeGI's ability to measure heterogeneous sources in the near field, placed directly on the detector's faceplate, to perform isotopic mapping useful to nuclear forensic missions. The intrinsic efficiency is strongly dependent on where the photons interact within the germanium. The efficiency was mapped using a collimated beam of ^{154}Eu photons measured at 108 locations spanning the detector's face. This data set was then fit with a univariate quadratic function to interpolate the efficiency at any point on the detector's face. This allows the efficiency at any location to be calculated, which is paramount for making measurements with the most accuracy possible. The position and energy dependence are uncorrelated and thus the absolute efficiency at any position and for any gamma-ray energy can be calculated by the convolution of the spatial and energy efficiencies. Also, after an initial in-laboratory calibration, the field calibration can be reduced to a single measurement. The efficiency varies by 6-20% within the sensitive volume of the detector.

To better understand experimental results, the GeGI was simulated with ANSYS Maxwell R18.2 to model the electric fields and a custom charged particle transport code to determine the charge collection as a function of gamma-ray interaction location. The simulations resulted in the creation of a dimensionless number, ψ, that is linear and unique as a function of the induced currents on neighboring electrodes. Using ψ, the

location of the event at a sub-strip level can be calculated with greater precision than is possible with the GeGI's base software. This feeds into the known spatially dependent intrinsic efficiency previously measured within the GeGI. By improving the sub-strip event localization, and using the correct positon dependent efficiency, the ability to quantify a source is improved by up to 20%.

DEDICATION

This thesis is dedicated to my mother: she only saw the beginning of my journey, but I know she would have supported me through its entirety.

ACKNOWLEDGEMENTS

I would first like to thank my committee chair, Dr. Marianno for not giving up on me through this process. I did not make it easy, but he supported me through it all. I would also like to thank Dr. James Fast, formerly of Pacific Northwest National Laboratory. Working with him at PNNL was an absolute pleasure and I like to think I learned at least half of what he tried to teach me. Finally, I would like to thank Dr. Sarah Sarnoski for keeping me sane while we shared a cubical together at PNNL.

I would also like to thank my thesis committee; Dr. Marvin Adams, Dr. Sunil Chirayath, and Dr. Sunil Khatri; for their helpful comments throughout this process.

CONTRIBUTORS AND FUNDING SOURCES

Contributors

This work was supervised by a thesis committee consisting of Professor Marianno, Adams, and Chirayath of the Department of Nuclear Engineering and Professor Khatri of the Department of Electrical & Computer Engineering. Dr. James Fast of the Thomas Jefferson National Accelerator Facility provided valuable insight and assistance throughout.

All other work conducted for the thesis was completed by the student independently.

Funding Sources

Graduate study was supported by a fellowship from Texas A&M University and a research fellowship from the South Carolina University Research and Education Foundation.

This material is based upon work supported by the U.S. Department of Homeland Security under Grant Award Number 2012-DN-130-NF0001-02. Its contents are solely the responsibility of the authors and do not necessarily represent the official views of the Department of Homeland Security.

TABLE OF CONTENTS

Page

LIST OF FIGURES

Page

LIST OF TABLES

Page

1. INTRODUCTION

In 2010 House Resolution 730, titled *Nuclear Forensics and Attribution Act* was passed [1]. Within this bill, the United States Congress found that "in order to identify special nuclear material and other radioactive materials confidently, it is necessary to have a robust capability to acquire samples in a timely manner, analyze and characterize samples, and compare samples against known signatures of nuclear and radiological material". Many samples produced directly by the detonation of a nuclear device will have short half-lives, and thus timely acquisition and measurement of the samples are of the utmost importance.

The International Atomic Energy Agency (IAEA) has published a suggested plan of action in the case that a nuclear forensic investigation is ever necessary. This plan includes the recommended immediate steps as well as a timeline of suggested scientific analyses to be performed [2]. Although this plan is explicitly for samples interdicted during illicit trafficking, it can broadly be applied to the analysis of any unknown sample.

After determining a nuclear forensic investigation is necessary, the first step is to determine the radiation hazard as well as any other safety concerns. Then samples are collected and measured using mobile nondestructive assay (NDA) for on-site categorization. Based on the sample categorization, they are sent to national laboratories that have the capabilities to perform the necessary analyses. [2]

The current methods of immediate sample characterization are limited to gross radiation counting, gamma-ray spectroscopy, and macroscale physical characteristics. Although physical characteristics may give clues to the heterogeneity of the samples, none of the initial sample characterization techniques can provide information as to the distribution of the radionuclides within the sample.

As will be discussed later in this thesis, the spatial distribution of radionuclides within a heterogeneous source provides important information for nuclear forensic analysis. It is the goal of this work to analyze the application of a commercial off-the-shelf detector for use in a new method to enhance the current methods of nuclear forensic analysis. The results of this research will be an understanding if a portable germanium detector is a candidate to quickly triage nuclear forensic samples by spatially mapping the isotopes.

1.1. References

1. "Nuclear Forensics and Attribution Act," One Hundred Eleventh Congress of the United States of America, 2010.
2. "Nuclear Forensics Support Reference Manual," in "IAEA Nuclear Security Series," International Atomic Energy Agency, Vienna, Austria, 2006.

2. CORRECTING FOR SPATIALLY DEPENDENT INTRINSIC EFFICIENCY OF A GERMANIUM DOUBLE SIDED STRIP DETECTOR TO IMPROVE NULCEAR FORENSICS RESPONSE

2.1. Introduction

There are three primary modalities in which most radiation detectors are used. The first is simple detection: determining if radiation is present or not. The second is radio-isotope identification and quantification of a source. The final is isolation, to be able to discriminate a specific radiation source at a specific location from a field of background. Imaging detectors focus on the location of radiation sources and are primarily used in either medical procedures or far-field measurements [1]. Far-field measurements are where the radiation source is typically several meters away and the goal is to isolate a radioactive source in a wide region of background radiation.

This research investigates an innovative, new way to use imaging germanium detectors for near-field imaging. The goal is to take a heterogeneous radiation source, place it directly on the face of the detector, and then use the detector's imaging capability to quantitatively map the isotopic heterogeneities within the source. This "quantitative isotopic mapping" of a heterogeneous source requires that the detector's response as a function of photon interaction location be quantified.

Developing a methodology for quantitative isotopic mapping would be an improvement in the realm of immediate, nondestructive, sample characterization. The current methods of immediate sample characterization are limited to gross radiation

counting, gamma-ray spectroscopy, and macroscale physical characteristics. Although physical characteristics may give clues to the heterogeneity of the sample, none of the initial sample characterization techniques can provide information as to the distribution of radionuclides within the sample. Congress has recommended that new methods be developed to complement or replace existing techniques [2]. Understanding the spatial distribution of radionuclides within a heterogeneous source is relevant for nuclear forensic analysis. It is the goal of this research to advance the state of the art of isotopic radionuclide mapping with spatially resolved High Purity Germanium (HPGe) gamma-ray spectroscopy for the specific purpose of reducing the time of nuclear forensic analysis. The results of this research will be an improvement to a mechanically-cooled high purity germanium detector to quickly triage nuclear forensic samples by spatially mapping the isotopes, a feat that has never been demonstrated.

The standard methodology of efficiency calibration uses a single point source that uniformly irradiates the entirety of the detecting sensor. This results in an average efficiency for a photon that interacts anywhere within the detector. Initial measurements with the Germanium Gamma-ray Imager (GeGI) found that the detector's efficiency, measured with a collimated beam at different locations on the germanium crystal, had greater than 20% variation [3]. A singular, average, efficiency would therefore provide incorrect quantitative results in the near-field imaging regime because the source photons are limited to small regions of the detector rather than interacting with the full detector volume. In order to accurately perform near-field quantitative imaging, the

efficiency variation as a function of event location must first be understood and calibrated.

To make quantitative measurements, which is the ultimate goal, requires a calibrated detector. A traditional efficiency converts number of events into activity or mass. This work is the same, but without averaging the detector response over the full detector volume. The detector's response was measured on the smallest physical scale possible by using a highly collimated beam of photons to interrogate the germanium. Approximately 40% of the detector was interrogated, and the remaining detector response was interpolated based on these measurements. The efficiency was calculated in three parts. The first, and simplest was the energy dependence. Then the pixel level spatial dependence and finally sub-pixel level spatial dependence. When using imaging HPGe detectors for forensic applications in the future, the spectrum will be split over three dimensions (two spatial, one energy) and will have three levels of efficiency correction applied to create a map of activity, or mass, as a function of location.

2.1.1. Background Information: Planar Germanium Detectors

Germanium detectors have been used for decades as the standard for measuring photon radiation because of their unrivaled energy resolution. They have limited disadvantages, including the requirement to operate at temperatures below 100 K and high cost. While the most common geometry for germanium detectors is that of the semi-coaxial, the planar geometry is simpler when it comes to position sensitive measurements because of its more uniform electric field [4]. Modern planar detectors

have electrode strips placed on the front and back face of the detector (Figure 1). When these electrodes are placed orthogonally to each other they can then be used to determine the location of the energy deposition. When a photon interacts within the germanium, it will create a cloud of electrons and holes. These charges will follow the electric field lines and be drawn to the nearest oppositely charged electrode. This results in charge deposited on a single electrode strip on both the front and back face of the detector. The gaps between the strips act as guides for the charged particles so that the charge will be collected on the strips directly above and below the event. For any two separate strips that have charge, there is only one location that the event could have occurred because of the orthogonality of the strips [5]. The charges, both electrons and holes, will be drawn to the nearest oppositely charged electrode. This isolates the position of the interaction to an area equal to the square of the strip width.

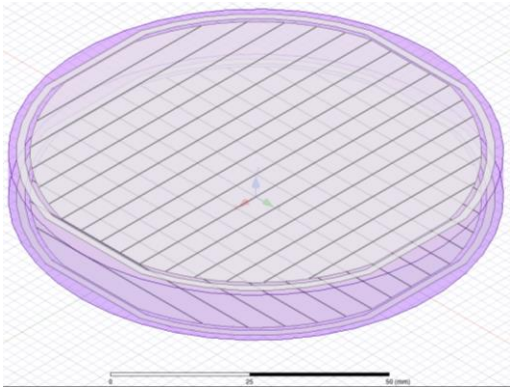

Figure 1. A transparent view showing the orthogonal strips on the back of the germanium.

The earliest reference to using germanium-based semiconductor detectors for imaging purposes was by Parker et al. in 1969 [6]. Before 1969, the primary method of imaging was with scintillator-based detectors. Parker et al. investigated two methods of designing a lithium-drifted germanium detector to provide position sensitivity. The first was the "stalactite" array in which there were a large number of germanium stalactites, each with individual electronic read-outs. This method was inferior, primarily because of the electronic complexity, to the orthogonal strip design. This design used a block of lithium-drifted germanium and had parallel grooves etched on the front and back face such that the two faces had orthogonal etching. This design could localize an event to within a 2 mm × 2 mm square with energy resolution of 6.5% at 122 keV. [6]

The first germanium gamma-ray imagers focused on medical imaging, but they have also been used in astronomy [7] and a variety of basic physics projects [8-10]. Most recently, the push for improvements in spatially resolved germanium detectors have come from M. Amman and P. Luke. In 2000, they demonstrated three-dimensional spatial sensitivity with an orthogonal-strip germanium detector; they inferred depth of interaction based on the time of charge collection [5]. Amman and Luke also used field shaping electrodes to reduce incomplete charge collection [5] and amorphous germanium contacts to improve the fabrication process [11] resulting in detectors that were more accurate and easier to produce.

PHDS Co. has been developing a family of portable Germanium Gamma-ray Imagers (GeGI) [12]. The GeGI is a planar, Double Sided Strip Detector (DSSD). Recently they have developed a variant (GeGI-s) that is capable of several million

counts per second distributed across the whole detector. This high count-rate capability allows high-activity samples to be placed directly on the face of the detector without significant dead time losses. Currently, if a source has high activity it must be distanced from the detector such that dead time, which makes it difficult for software and electronics to compensate for quantifying a sample, is minimized. The further a source is from the detector the more point-like it appears; this means that high activity sources cannot be imaged in the near field with traditional imaging detectors. One potential method to overcome this is through the pinhole imaging technique [1], whereby the source is significantly collimated down to under a millimeter-squared. This reduces the detection probability because only a small region of the source is actively measured at one time. Ultimately, this would then allow high activity sources to be measured, however it increases the total imaging time as only small regions can be measured at any given time.

A representative geometry of the detector is produced in Figure 2. The strips are orthogonal in nature which create three types of event location. The first, and most common, is for events that occur when two strips fully overlap. A representative location of where this could occur is given by the star on Figure 2. The second type of event occurs in the gap between two strips on one face of the detector, but on the full strip on the opposite side of the detector (triangle). The final, and most rare, event is the “true” gap (diamond). These are the events that occur in the small space that is a gap between strips on both sides of the detector. In terms of nomenclature, a “pixel” is the volume in which there is full overlap from strips on both sides of the detector and is not indicative

of the minimum spatial resolution achievable. Although it is possible to determine the depth of an interaction, this work does not segment the pixels into sub-regions based on depth, commonly called voxels. Therefore Figure 2 has nine pixels.

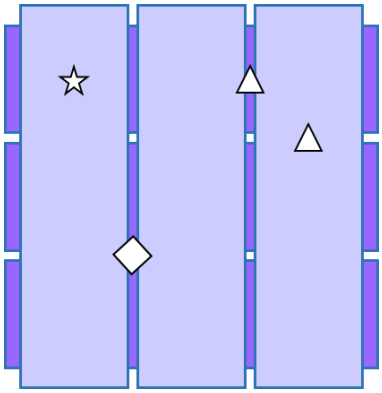

Figure 2. A representation of the detector's strip nature. This is not to scale and the gaps are exaggerated.

2.2. Materials and Methods

2.2.1. The GeGI Detector

The measurements were made with a PHDS Co. GeGI-s detector [12]. The GeGI-s is a segmented, planar, HPGe detector based on the GeGI-4. The crystal is 90 mm in diameter and 10 mm thick. There are 16 strips on the front of the detector, and 16 orthogonal strips on the back of the detector; the pitch is 5 mm and there is a 0.25 mm gap between strips. Therefore, a single pixel is 4.75 mm × 4.75 mm. The "s" version of GeGI has been uniquely modified for operation at high rates, considered greater than 20,000 s^{-1}.

2.2.2. Collimator System

The front face of the detector was placed against a collimator, and the collimator was affixed to a three-axis translation stage with a precision of 25 μm. The collimator was made of tungsten with a copper faceplate and lead side plates. The copper plate reduced the tungsten x-ray flux seen by the detector, and the lead provided shielding to prevent leakage along a seam in the tungsten. The block of tungsten had a primary borehole drilled through it with a radius of 2.5 mm. This borehole was filled with two tungsten plugs of smaller diameter to further collimate the photon beam. This resulted in a borehole radius of approximately 0.5 mm. The face of the GeGI was placed directly against the copper plate. It was approximately 10 mm from the outer edge of the GeGI to the germanium crystal. Between the aluminum front window and the germanium was another layer of aluminum to reduce infrared radiation. The overall thickness of aluminum, counting the front window and infrared shield, was approximately 1 mm.

The beam profile was calculated using the integral form of the transport equation. Understanding the beam profile of the collimator system was very important for correct interpretation of the experimental results. For the geometry of this system, the uncollided photon beam profile was uniform with no significant beam broadening from the end of the collimator to the germanium crystal, thus the beam width was equivalent to the width of the borehole. However, the total flux was less uniform due to scattered photons. The impact of scattered photons was not determined as the analyses focused on photopeaks.

2.2.3. Normalized Efficiency

The absolute or total efficiency of a detector is the product of the geometric acceptance, the probability of a photon to reach the detector, with the intrinsic efficiency, the probability of a photon to interact within the detector volume [4]. From this characteristic feature, one can convert the events measured into source activity. A Europium-154 source was placed within the collimator system to create a beam of photons. The detector was positioned in front of the collimator such that the collimator's range of motion could fully cover the germanium. The distance from the source to the detector was 10 cm. To assure the efficiency was determined at specific points on the detector face, the collimator was rastered, moving the beam of photons across the face of the detector, to probe the detector response as a function of interaction location. Starting with the definition of absolute efficiency from [4],

$$\epsilon_{\mathrm{abs}} = \epsilon_{\mathrm{geo}}\epsilon_{\mathrm{int}} = 100 \times \frac{C}{N}, \qquad \text{(Eq. 1)}$$

where ϵ is the efficiency, either the absolute (abs), geometric (geo), or intrinsic (int). The counts in the full energy peak, less background, is C, and N is the total number of photons emitted by the source during the live counting time.

The normalized efficiency,ϵ_n is defined by the absolute efficiency at any location (x, y) normalized by the efficiency at the center of the detector, subscript zero. This variable was created to more easily compare the variation in efficiency as a function of beam location.

$$\epsilon_{\mathrm{n}}(x,y) = \frac{\epsilon_{\mathrm{abs}}(x,y)}{\epsilon_{\mathrm{abs,0}}} = \frac{\epsilon_{\mathrm{geo}}\epsilon_{\mathrm{int}}(x,y)}{\epsilon_{\mathrm{geo}}\epsilon_{\mathrm{int,0}}} = \frac{100 \times \frac{C(x,y)}{N}}{100 \times \frac{C_0}{N}} \qquad \text{(Eq. 2)}$$

Assuming that the source has not decayed significantly between the two measurements, that the measurement times are the same, and that the geometry is unaltered, the normalized efficiency is more simply calculated by the ratio of the counts, either for a single photopeak or the entire spectrum,

$$\epsilon_n(x,y) = \frac{\epsilon_{abs}(x,y)}{\epsilon_{abs,0}} = \frac{C(x,y)}{C_0}. \qquad \text{(Eq. 3)}$$

2.2.4. Fine Raster

The location of the germanium and conductor strips within the GeGI were not perfectly known, so the first measurements focused on orienting the collimator with the germanium. The photon beam was finely rastered, both vertically and horizontally, in order to find the strip centers as well as the gaps between strips. Finding the strip centers, and knowing the strip pitch, the location of all strip centers and strip gaps were calculated. All presented results are in detector coordinates, such that the detector horizontally and vertically spans 0 to 80 mm, with the strip centers falling at 2.5, 5.0, 7.5 mm, etc.

2.2.5. Coarse Raster

Three different measurement lengths were used to achieve different levels of statistical precision. The first data set, forty-three discreet four-hour measurements at different collimator positions, covered the primary horizontal and vertical axes and the

diagonal axes. Whereas the remaining sixty-five measurements, the second data set, lasted for 1 hour each. The second data set had a shorter count time in order to measure a greater quantity of locations. The measurement uncertainty achieved with 1-hour measurements on the total collected counts was approximately 1%. The longest measurements were 13 hours each, the third data set, and provided the best statistics for the high energy ^{154}Eu peaks.

2.2.6. Event Selection

The total collected data was down selected to analyze only relevant events. First, the events below 30 keV were removed. While the GeGI can measure photons down to 10 keV, the lowest energy gamma-ray was 123 keV and thus none of the low energy events were meaningful in this experimental campaign. Second, when calculating the normalized efficiency, the data were limited to a single pixel. Raw data from the GeGI allows for for individual pixel analysis. At each measurement location the collimator focused the photon beam, which is smaller than a single strip, to the center of a strip. Therefore, any events on pixels outside of the primary pixel were either from background, or non-collimated source photons and the result of a Compton scatter. The recorded events outside of the primary pixel are Compton dominated. The single, primary pixel had approximately 20% of the events compared to the full detector even though it is only 0.5% of the detector's volume. Third, events that had multiple interactions were removed. Over the full detector volume, approximately 10% of the total events are from multiple scatters. The other 90% are single site events, either

depositing their energy in a single photoelectric interaction or Compton scattering a single time and then leaving the germanium. However, when considering just the primary pixel rather than the full detector volume, multi-site events account for only 4% of the total events because the collimator provides shielding from background radiation. Most of the multi-site events therefore did not contribute to the photopeaks of the spectrum and do not contribute to the analysis of spatial efficiency. Choosing not to include multi-site events simplified the associated physics analysis and did not affect the statistical certainty from which conclusions were drawn.

Removing events with multiple scatters had a secondary effect of removing a "satellite" peak that had appeared on the high energy shoulder of the highest energy photopeaks. It was previously discovered that the primary contribution to the satellite peaks is due to energy sharing between neighboring strips [13]. During any event, a small amount of the charge is deposited (via capacitive coupling) on the two adjacent strips. In the case of an event that is only measured on a single strip the standard calibration accounts for this and the correct energy is recorded. However, when a multi-site event occurs on two neighboring strips, half of the energy that was assumed lost was actually recovered and double-counted. This results in a recorded energy deposition that was higher than the true energy deposition. These events can be recovered as the double counting of charge is linear with incident photon energy. Therefore, when an event occurs that has multiple scatters between neighboring strips its total energy must be reduced by 0.3%.

2.3. Results

2.3.1. Fine Raster

In order to calibrate the collimator's location against the location of the germanium strip grid, a series of measurements were made. Thirty horizontal and thirteen vertical measurements were made and between each measurement the photon beam was displaced by $1/12^{th}$ of the strip pitch, 0.42 mm. The fine movement showed the gap between strips, located the strip center, and showed that neighboring strips will record events before the photon beam reaches it. Each of the four datasets plotted in Figure 3 are the response of a single pixel as a function of the photon beam's location. Three of the data sets are a horizontal raster traversing three neighboring strips. The fourth data set is of a vertically rastered pixel. Even when the beam is focused on a single strip, events are measured on the neighboring strips. This could be explained by imperfect collimation of the photons, as the spectra displays distinct photopeaks. This was not due to scattering because the data set was limited to single-site events. The bottom plot of Figure 3 was created by summing the detector's response from all three horizontal pixels at each individual beam location and then calculating the normalized efficiency from this summed response.

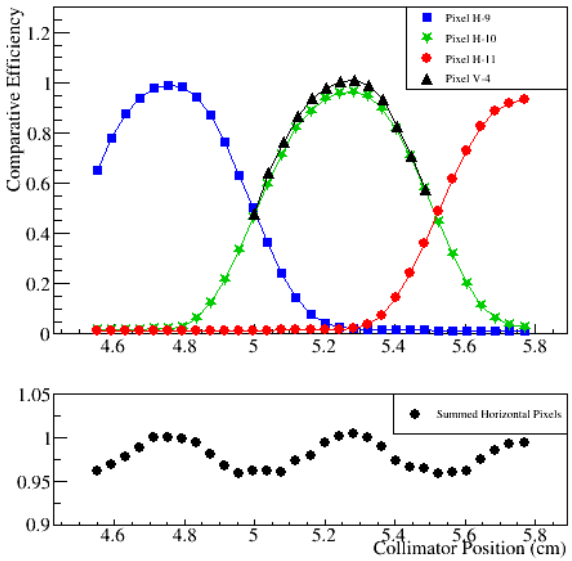

Figure 3. The top plot shows the normalized efficiency for neighboring pixels at 30 different photon beam locations, whereas the bottom plot shows the sum of all three pixel responses.

For any single pixel there is a reduction in normalized efficiency of almost 50% within the gaps between pixels. The summation of neighbor pixels recovers some of this loss in efficiency, however there is still a total reduction in normalized efficiency of approximately 5% within the gap between pixels compared to the pixel center. It is also worthy to note that the region of reduced normalized efficiency is wider than a single gap, 1.25 mm as opposed to 0.25 mm. This shows that the detector is most sensitive in the center of the pixels, and sources that span multiple pixels will have to be corrected for the loss in normalized efficiency in the gaps between pixels.

It was found that the edge-most strips had significantly worse efficiency than those at the center of the detector. A fine raster was performed over the two edge-most

strips to see how the efficiency reduces towards the edge of the germanium. Of the 16 pixels that span the width of the detector, the second and fifteenth, penultimate, pixels had a lower normalized efficiency than the detector center, but the shape of the normalized efficiency as a function of position across the pixel was the same as the center. This can be seen by comparing Figure 3 and Figure 4. The edge-most pixel was approximately 40% as efficient as its neighbor, the penultimate pixel, and also has a different shape. This effect is suspected to be due to the non-uniformities in the electric field at the edge of the detector, stemming from the grounding of the applied voltage by the guard ring.

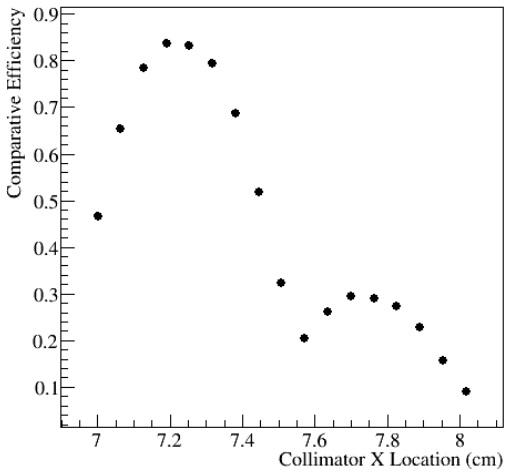

Figure 4. The normalized efficiency of a fine raster of the photon beam over the edge-most two strips of the germanium. The 1-σ error bars are plotted but smaller than the markers.

2.3.2. Coarse Raster

The face of the detector was systematically studied to understand the variations in normalized efficiency. The beam was focused on pixels across the detector with the aim of creating a predictive fit to the spatially variant normalized efficiency. In total, 108 pixels were interrogated with photons to measure the detector response. Normalized efficiency is shown in Figure 5. The efficiency of the edge most strips is approximately one-third that of the detector's center, as mentioned before, this is suspected to be caused from the non-uniform electric field at the edges of the detector. The variation in detector efficiency across the face of the detector was unexpected and has not been presented before in the literature. It is a common assumption that the detector's response is uniform, and that variation seen across the detector comes mainly from a non-uniform photon field rather than the detector response. The importance of this discovery is that measurements of activity made of sources that are both small and close to the detector will be incorrect because the efficiency used is a detector average and does not account for the variation as a function of space.

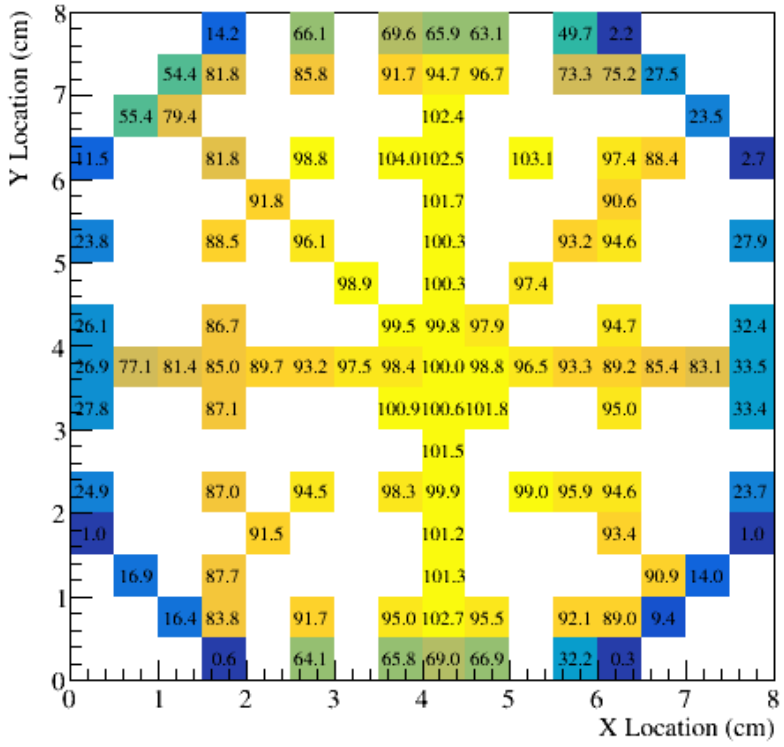

Figure 5. The normalized efficiency at all of the measured pixels. The geometric center of the detector is in a true gap and thus the nominal central pixel with regards to normalizations is off center.

The efficiency as a function of two-dimensions was fit with a surface to allow interpolation between the measured locations. The functional dependence of the surface fit was determined by the primary horizontal and vertical strips. The primary horizontal axis, Figure 6a, is quadratic in nature (R^2=0.99), barring the edge most pixels. The primary vertical axis, Figure 6b, can be fit by a quadratic function, however it is concave rather than convex and the quadratic coefficient is smaller by a factor of 50. It also has a much lower coefficient of determination (R^2=0.47), which is indicative of the data

having a weak function dependence with position; no other function was found to have a better R^2. The charge collection only occurs on the strip where the interaction took place, so when the beam travels vertically each measurement is being read-out along the same channel and the normalized efficiency has less variation. However, the horizontal raster has each measurement being read out by a different strip of diminishing length as the beam nears the edge and the shorter strips result in lower efficiency. This is not a dead time issue as the overall count rate during these photon beam studies was 245.60 ± 0.02 s^{-1}. The GeGI detector is designed to measure high rate scenarios, (>20,000 s^{-1}) without spectral degradation and thus there is no chance that this result stems from the detector being paralyzed and missing 20% of the events.

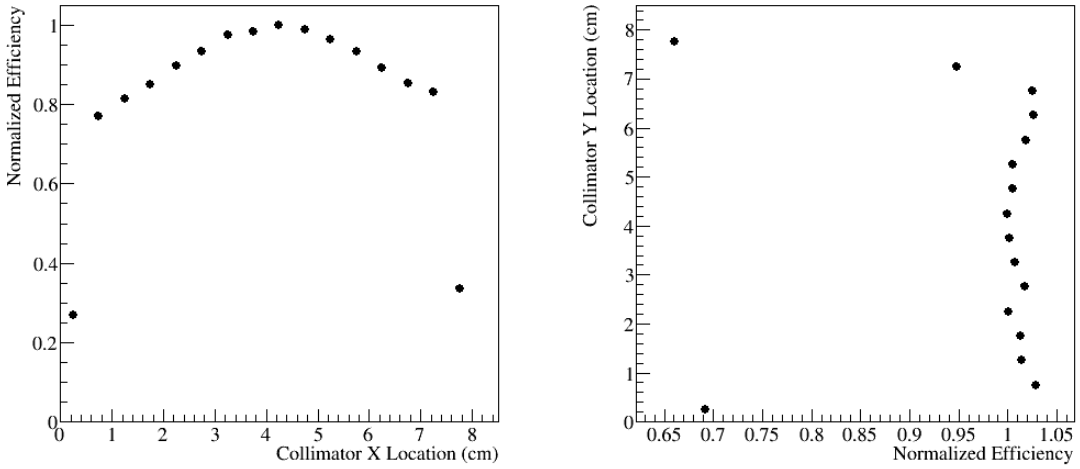

(a) (b)

Figure 6. The primary horizontal (a) and vertical (b) normalized efficiencies. The uncertainties are smaller than the data points.

The functional dependences of the horizontal and vertical axes were combined in Eq. 4 as a bivariate quadratic to calculate the normalized efficiency for any pixel on the detector. However, in fitting the bivariate quadratic to the data, all fitting parameters involving the vertical component had uncertainties larger than the fitting parameters, indicating that these parameters were not statistically significant. This reduces the bivariate quadratic to a univariate quadratic. The fitting coefficients for both the bivariate and univariate fits are presented in Table 1. The univariate form of Eq. 4, which has no vertical dependence, describes the surface shown in Figure 7. The surface fit has a coefficient of determination, R^2, value of 0.897. The fit was limited to the center of the detector, $x, y \in [1,7]$ cm, as no continuous function was found to describe the precipitous drop at the edge of the detector.

$$\epsilon_n(x,y) = C_1x^2 + C_2y^2 + C_3x + C_4y + C_5xy + C_6 \qquad \text{(Eq. 4)}$$

Table 1. Fitting parameters for Eq. 4

	Bivariate Fit		Univariate Fit	
Parameter	Value	Uncertainty	Value	Uncertainty
C_1	-2.18	0.52	-2.14	0.51
C_2	0.32	0.54	0	0
C_3	18.64	4.79	18.54	4.18
C_4	-2.79	5.01	0	0
C_5	0.07	0.47	0	0
C_6	64.98	13.92	60.42	7.66

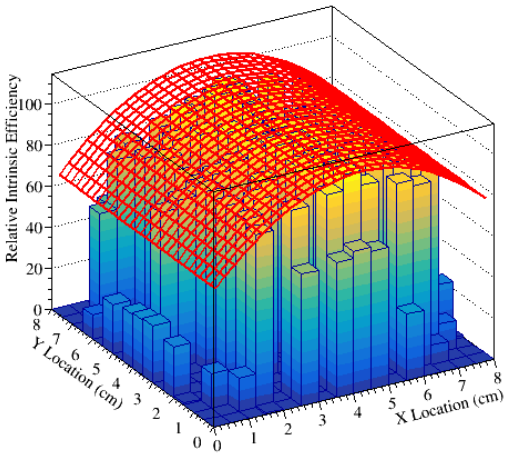

Figure 7. The 2-D surface fit to the normalized efficiency.

This surface describes the variation of normalized efficiency across the whole detector of the pixel centers, and the average of the surface, $\bar{\epsilon_n} = 93.92\%$, would be equivalent to the detectors bulk efficiency normalized by its area and efficiency at the center of the detector. Comparing the average normalized efficiency, $\bar{\epsilon_n}$, to the true normalized efficiency at any location, $\epsilon_n(x, y)$, gives the error when measuring a sample that is primarily measured by only a few pixels. In the center of the detector the calculated source activity would be off from the true value on average by 6%. However, it could be different by up to 20% if the source being measured is small and not located on the center of the germanium.

Collecting the data necessary for a map of normalized efficiencies is impractical to repeat with regularity and would not be possible outside of the laboratory setting. However, it is a standard practice to check the bulk efficiency and energy calibration of a detector with a point radiation source at sufficient distance to present a uniform

radiation field. Connecting the map of normalized efficiency to a flat field measurement would allow a much simpler method of checking the spatial efficiency before measurements.

By rearranging the definition of normalized efficiency, the absolute efficiency at any position x, y can be calculated based on the absolute efficiency at the center of the detector and the normalized efficiency at the position (x, y).

$$\epsilon_{\mathrm{n}}(x,y) = \frac{\epsilon_{\mathrm{abs}}(x,y)}{\epsilon_{\mathrm{abs,0}}} \rightarrow \epsilon_{\mathrm{abs}}(x,y) = \epsilon_{\mathrm{abs,0}}\epsilon_{\mathrm{n}}(x,y) \qquad \text{(Eq. 5)}$$

Integrating the normalized efficiency surface over the detector's area, A, yields the sum of all normalized efficiencies over the detector's center. This is the total number of counts that each pixel would register if the collimator focused on each of the central pixels divided by the events measured in the center of the detector. Dividing this integral by the area of the detector is then equal to the average normalized efficiency, a known quantity.

$$\bar{\epsilon_n} = \frac{\iint \mathrm{d}A\ \epsilon_{\mathrm{n}}(x,y)}{\iint \mathrm{d}A} = \frac{\iint \mathrm{d}A\ \epsilon_{\mathrm{abs}}(x,y)/\epsilon_{\mathrm{abs,0}}}{A} \rightarrow \epsilon_{abs,0} = \frac{\iint \mathrm{d}A\ \epsilon_{\mathrm{abs}}(x,y)}{A\bar{\epsilon}_{\mathrm{n}}} \qquad \text{(Eq. 6)}$$

And let

$$\epsilon_{\mathrm{abs,bulk}} = \iint \mathrm{d}A\ \epsilon_{\mathrm{abs}}(x,y) \qquad \text{(Eq. 7)}$$

Where, $\epsilon_{abs,bulk}$ is the bulk detector efficiency. By combining the definition of normalized efficiency, Eq. 3, and the above equation, the absolute efficiency at any position can be obtained once one knows the normalized efficiency map, Eq. 4, the average normalized efficiency, and the bulk detector efficiency.

$$\epsilon_{abs}(x,y) = \frac{\epsilon_{abs,bulk} \times \epsilon_n(x,y)}{A \times \bar{\epsilon_n}} \quad \text{(Eq. 8)}$$

Each detector that will be used in this manner will need to be laboratory calibrated before it can be used to its full extent in the field. The detector's response at a number of different pixels will be measured by collecting the spectrum from a collimated polyenergetic source. This work, being the first of its kind, measured over 100 locations but that would not be necessary to repeat. The normalized efficiency map could be replicated with fewer measurements with minimal loss of precision. Recalculating $\epsilon_n(x,y)$ with 23 measurements, just the primary horizontal and vertical axes, yielded a surface that was within 2% of the original for all but the boundaries. At the boundaries there was a 4.9% difference between the two $\epsilon_n(x,y)$ surfaces. From these measurements, the normalized efficiency map and its average can be calculated by taking the total counts within the collected spectrum from each pixel. With these measurements, only a single bulk measurement in the field would be needed to ensure that the spatial calibration has not changed.

2.3.3. Energy Dependence

Knowing that the efficiency of the detector is spatially dependent, it is important to determine if the normalized efficiency was energy dependent beyond the normal reduction in efficiency as a function of energy. Spectra were collected with the collimated ^{154}Eu source focused on a single pixel at the detector's center, the horizontal edge, and the vertical edge for 13 hours each. In each spectrum, the eight primary photons from the ^{154}Eu source were fit to a Gaussian with a linear background

subtraction using the ROOT fitting tools [14]. The Gaussian was modified such that the peak area was used as a fitting parameter rather than fitting to the peak height. Three separate energy efficiency curves, one for each pixel measured, were fit to these eight peak areas, all with $R^2 > 0.999$, by a modified asymmetric sigmoidal function, Eq. 9, and one such curve is shown in Figure 8. This equation is used rather than the standard method, [4], as it provides more realistic extrapolation at high and low energies. At high energies, above 2000 keV, it remains linear and at low energies the function approaches zero. No gamma-ray energies below 100 keV or above 2000 keV were used for calibration and thus the low and high energy extrapolation are not plotted in Figure 8.

$$\varepsilon(E) = \frac{A\left(1 - \frac{1}{1 + E^{-w_1}}\right)}{1 + \exp\left(\frac{\mu - \log E}{w_2}\right)} \qquad \text{(Eq. 9)}$$

A is a scaling parameter, E is the energy in keV, and μ, w_1, and w_2 are shaping constants.

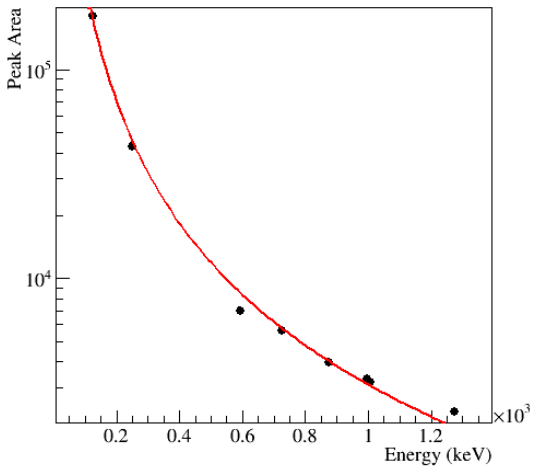

Figure 8. The energy efficiency curve of the GeGI detector as measured within the central pixel of the detector, all data points have uncertainty smaller than the size of the marker.

The photopeak areas were then used to calculate the normalized efficiency for each of the eight individual energies emitted by the ^{154}Eu. Figure 9 shows a comparison of the normalized efficiency, calculated for each photopeak, between the horizontal edge (blue stars) and vertical edge (red triangles) of the detector. The dashed colored lines are the averages over all energy for the horizontal and vertical edges, the dashed black line is unity and represents the normalized efficiency at the detector's center. The measurement uncertainty primarily stems from the number of events above background within a photopeak, which is a function of the branching ratio for the different photons and the intrinsic efficiency of the germanium. As expected from previous measurements, Figure 6, the horizontal normalized efficiency is approximately 80% of the central and vertical measurements.

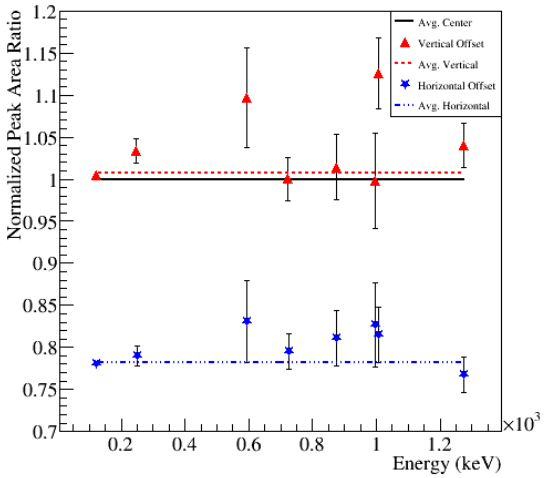

Figure 9. The photopeak areas at the displacement locations relative to the center.

The energy dependent normalized efficiency yields three conclusions. The first is that there is no significant energy-spatial correlation. The change in efficiency as a result of physical displacement of the photon beam does not have any energy dependence and is, within uncertainty, equivalent to the total normalized efficiency measured at that location. On an electronics level, the only difference between photons of different energy is the number of electron-hole pairs that are created. This indicates that the normalized efficiency is not dependent, or related to, the quantity of charge collected by the electrodes. The energy efficiency curves, measured at three locations, all had the same shape and were normal for a germanium detector. The second is that, even though the total normalized efficiency is significantly different for the horizontal and vertical displacements, both locations respond similarly as a function of energy. The third conclusion is that the uncertainty weighted average of all eight photopeaks provides a similar normalized efficiency to the normalized efficiency over all energies.

The vertical edge has a photopeak average normalized efficiency of 1.01 ± 0.003, and the horizontal edge's photopeak average is 0.78 ± 0.002. The normalized efficiency at those two locations calculated over the full energy spectrum were 1.01 ± 0.001 and 0.85 ± 0.001, respectively.

A similar analysis was applied to fine raster data comparing four locations across a single pixel and is shown in Figure 10. The results of the fine raster mirrored the conclusions of the coarse raster. The reduction in normalized efficiency is a function of space and not energy, the change in efficiency as a function of position across a single pixel is statistically significant, and the normalized efficiency at any given energy is equivalent to the normalized efficiency at that location for all energies. It should be noted that the detector still experienced the expected reduction of intrinsic efficiency with increasing photon energy. However that intrinsic effect is not apparent in Figure 10 because the data points compare the same photon energy at the center of the detector. Because the normalized efficiency was shown to be energy independent, the spatial efficiency can be calculated from a single energy photon. Previously, normalized efficiency was calculated based on the total counts within a spectrum. Calculating normalized efficiency with just a single photopeak will reduce the impact of Compton scatter and background.

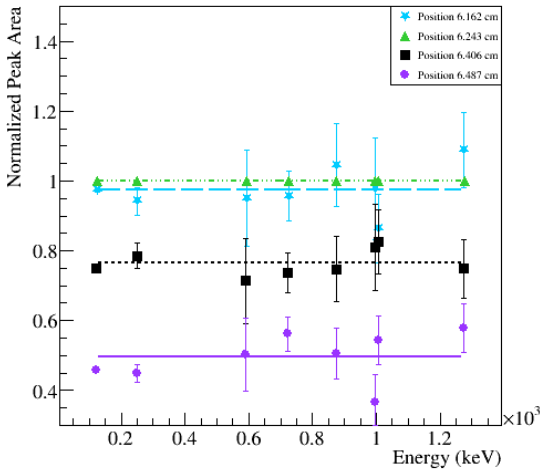

Figure 10. Four locations contained within a single pixel are compared to determine if the energy dependence exists on the fine scale as well as the coarse scale

2.4. Conclusion

The fact that the efficiency of the detector changes on the pixel level was expected from literature, but the fact that the efficiency changes across multiple electrode strips, and changes significantly, was unexpected. Precise measurements of the GeGI as a function of position has led to an understanding of its response, both on the pixel level and the sub-pixel level.

The spatial dependence of efficiency within the GeGI detector was unexpected at the coarse scale. The very edges of the detector had approximately one-third the efficiency of the detector center. This was not surprising because the lack of geometric uniformity, and the grounding strip, lead to a non-uniform electric field. But even a centimeter in from the edge strips, where the electric field should be uniform, there was a 20% reduction in efficiency. This effect was only noticeable in the horizontal direction

and not in the vertical direction. On the fine scale, looking at individual pixels, the vertical and horizontal efficiency changes are symmetric. The efficiency is reduced away from the center of the pixel in an almost quadratic fashion.

This research showed that the reduction in efficiency as a function of position is not related to the reduction in efficiency based on the energy of the photon. These can be treated therefore as independent quantities and the spatial efficiency can be calculated from a single low energy photon to yield the highest statistical precision. The spatial and energy efficiencies are then convolved to create a true absolute efficiency as a function of the photon's interaction location as well as the photons energy. Having calculated the spatially dependent normalized efficiency once with a collimated beam of photons, it is not necessary to repeat the measurement again. It has been shown that the absolute efficiency as a function of space is related to the bulk efficiency of the detector. Thus, a single bulk efficiency measurement in the field can be used to calibrate the detector for both its energy dependent and spatially dependent efficiency.

The spatially dependent efficiency proves an enhancement over the current strategy of calculating the efficiency based on a volume average. When calculating a samples activity this will result in an improvement by approximately 6—20% depending on the size of the sample and where on the face of the detector it is being measured.

2.5. References

1. R. C. Runkle, L. E. Smith, and A. J. Peurrung, "The photon haystack and emerging radiation detection technology," (in English), *Journal of Applied Physics,* vol. 106, no. 4, p. 041101, Aug 15 2009.
2. "Nuclear Forensics and Attribution Act," *One Hundred Eleventh Congress of the United States of America,* 2010.
3. T. W. Jacomb-Hood, S. E. Sarnoski, J. Fast, and C. M. Marianno, "Quantification of Spatially Variant Efficiency in an Orthogonal Strip Detector," in *Nuclear Materials Science, Processing and Signature Discovery Workshop,* Richland, Washington, 2018.
4. G. F. Knoll, *Radiation Detection and Measurement,* 4th ed. John Wiley & Sons, Inc., 2010.
5. M. Amman and P. N. Luke, "Three-dimensional position sensing and field shaping in orthogonal-strip germanium gamma-ray detectors," (in English), *Nuclear Instruments & Methods in Physics Research Section a-Accelerators Spectrometers Detectors and Associated Equipment,* vol. 452, no. 1-2, pp. 155-166, Sep 21 2000.
6. R. P. Parker, E. M. Gunnersen, J. L. Wankling, and R. Ellis, "A Semiconductor Gamma Camera with Quantitative Output. Preliminary Results," in *Symposium on Medical Radioisotope Scintigraphy*, Salzburg, Austria, 1968, pp. 71-85.
7. L. S. Varnell *et al.*, "A Position-Sensitive Germanium Detector for Gamma-Ray Astronomy," (in English), *Ieee Transactions on Nuclear Science,* vol. 31, no. 1, pp. 300-306, 1984.

8. R. A. Kroeger, W. N. Johnson, J. D. Kurfess, and B. F. Phlips, "Gamma ray polarimetry using a position sensitive germanium detector," (in English), *Nuclear Instruments & Methods in Physics Research Section a-Accelerators Spectrometers Detectors and Associated Equipment,* vol. 436, no. 1-2, pp. 165-169, Oct 21 1999.
9. J. H. Lee and C. S. Lee, "Polarization sensitivity and efficiency for a planar-type segmented germanium detector as a Compton polarimeter," (in English), *Nuclear Instruments & Methods in Physics Research Section a-Accelerators Spectrometers Detectors and Associated Equipment,* vol. 506, no. 1-2, pp. 125-133, Jun 21 2003.
10. A. Khaplanov, S. Tashenov, B. Cederwall, and G. Jaworski, "A gamma-ray polarimeter based on a single segmented planar HPGe detector," (in English), *Nuclear Instruments & Methods in Physics Research Section a-Accelerators Spectrometers Detectors and Associated Equipment,* vol. 593, no. 3, pp. 459-465, Aug 11 2008.
11. M. Amman, P. N. Luke, and S. E. Boggs, "Amorphous-semiconductor-contact germanium-based detectors for gamma-ray imaging and spectroscopy," (in English), *Nuclear Instruments & Methods in Physics Research Section a-Accelerators Spectrometers Detectors and Associated Equipment,* vol. 579, no. 2, pp. 886-890, Sep 1 2007.
12. E. Hull and M. Kiser, "Radioactive Threat Vision via Quantitative Gamma-ray Imaging," in *NCT CBRNe USA*, Washington D.C., 2016.
13. T. W. Jacomb-Hood *et al.*, "Spatially-resolved HPGe Gamma-ray Spectroscopy of Swipe Samples," in *58th Annual Meeting of the Institute for Nuclear Materials Management (INMM)*, Indian Wells, California, 2017.

14. R. Brun and F. Rademakers, "ROOT - An object oriented data analysis framework," (in English), *Nuclear Instruments & Methods in Physics Research Section a-Accelerators Spectrometers Detectors and Associated Equipment,* vol. 389, no. 1-2, pp. 81-86, Apr 11 1997.

3. CHARGED PARTICLE TRANSPORT SIMULATION OF A PLANAR, ORTHOGONAL STRIP HPGE

3.1. Introduction

Previously, the Germanium Gamma-ray Imager (GeGI) was efficiency calibrated in both the spatial and energy domains [1]. The GeGI is a High Purity Germanium (HPGe) Double Sided Strip Detector (DSSD) developed by PHDS Co. for far field imaging [2]. While the detector's response as a function of incident photon energy matched expectations for an HPGe [3] , the detector's intrinsic efficiency was dependent on the location of the gamma-ray interaction. This spatial dependence was not symmetric and occurred only with horizontal translation away from the detector's center. This spatially dependent efficiency was proved to be separate from, and unrelated to, the energy-dependence of the efficiency. Ultimately, a complete efficiency calibration of the GeGI detector requires two independent correction factors, one based on the energy of the event and the second based on the location of the event.

This paper continues the previous research with the GeGI by modeling the electron-hole transport within the detector and using those models to improve the position sensitivity of the GeGI. This begins with modeling the electric fields within the germanium, using the commercially available ANSYS Maxwell R18.2 software [4], to determine the velocity and Shockley-Ramo weighting fields of the charged particles. Then a custom charged particle transport simulation was carried out for the movement of charged particles through germanium. The Shockley-Ramo equation was solved to

determine the current induced on the primary electrode strip as well as neighboring strips. This induced current was then used to find a better methodology of event localization than is currently used by the GeGI software. This new method of event localization was then applied to real data collected with a GeGI detector to show an improvement in near-field imaging. The result is a more exact determination of the spatially dependent efficiency. The more precisely the position of the event is known, the more precisely the activity of the sample will be measured.

This is relevant in a nuclear forensics situation because sources of interest will be highly heterogeneous. Better event localization will result in an improved understanding of the spatial distribution of radionuclides within the source. Performing this analysis with a commercially available, portable HPGe will have an end result of improving the nuclear forensic timeline as samples could be quickly triaged to understand their heterogeneity.

3.2. Background Information

3.2.1. The GeGI Detector

The PHDS Co. GeGI are a family of planar, double sided strip detectors (DSSD) [2]. The GeGI-s, a modified version of the GeGI-4, is designed for operation at high count rates, considered greater than 20,000 s^{-1}. The germanium crystal is 90 mm in diameter and 10 mm thick. There are 16 orthogonally oriented electrodes per face. The electrode pitch is 5 mm with 0.25 mm gap between strips and an electrode guard ring at

the edge. The most important aspect of this detector is that its intrinsic efficiency varies spatially, shown in Figure 1.

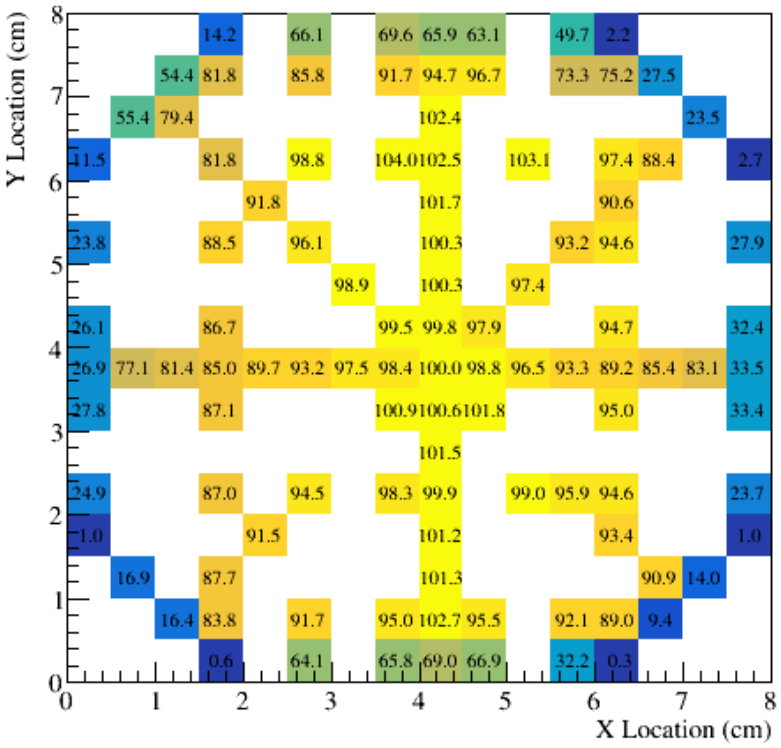

Figure 1. The normalized efficiency at all of the measured pixels. The geometric center of the detector is in a true gap and thus the central pixel with regards to normalizations is slightly off center. Reproduced from [1].

3.2.2. Finite Element Method

ANSYS Maxwell R18.2 is a commercial software product designed for electrostatic and electrodynamic simulations [4]. It uses the finite element method to transform the continuous partial differential Maxwell equations to a series of discreet algebraic equations [5]. The Finite Element Analysis (FEA) is done in four basic steps:

discretization of the domain, selection of the interpolation function, formulation of the system of equations, and solution of the system of equations.

Once the GeGI's geometry was modeled using ANSYS Maxwell R18.2, including material definitions and applied voltages, the FEA solution will discretize three-dimensional volumes into tetrahedrons, and two-dimensional into triangles. This discretization process will begin uniform, but as the solution iterates the regions of highest complexity will have a greater number of mesh elements. Ultimately, the smaller the mesh element the simpler, and more accurate, the solution but the higher the computational time. The interpolation function for Maxwell is a quadratic polynomial. This is because the greater the level of discretization the closer simple polynomials come to approximating the true solution to the Maxwell equations. The trial functions for every mesh element are then combined and solved simultaneously. The Galerkin method of solution assumes a solution to the boundary-value problem and then calculates a weighted residual between the original expression and the assumed solution [6]. Minimizing the residual leads to the best solution. It is also referred to as weighted residuals. The system of equations is iteratively solved, with each iteration further discretizing the space to reduce the solution uncertainty as needed. The discretization of space is non-uniform, resulting in a higher element density in the most complicated regions of space, to balance solution accuracy with computational cost.

3.2.3. Shockley-Ramo Theorem

The movement of charged particles within the GeGI's germanium crystal induces current on every electrode, and the magnitude of the induced current can be related to the initial gamma-ray interaction site. Shockley [7] and Ramo [8] independently derived an analytical solution to calculate how much current is induced by the movement of a charged particle.

The instantaneous induced current i is a function of the carrier charge, q, the carrier velocity, $\vec{v}$, and the weighting field, $\vec{E}_0$.

$$i = q\vec{v} \cdot \vec{E}_0 \qquad \text{(Eq. 2)}$$

When considering a strip detector, a moving charge will induce a current on every strip of the detector even though only one strip directly collects the charge. The induced current is strongest in the strips directly neighboring the collecting strip and will diminish with distance from the collecting strip. What the theorem refers to as the "weighting field" is not a true electric field, instead it is the field that would exist given specific non-realistic boundary conditions. The weighting field is calculated separately for each strip of the detector by setting artificial boundary conditions of 1 V on the strip in question and every other strip with 0 V. With these artificial boundary conditions in place, solving for the electric field instead yields the weighting field.

The true electric field is needed to calculate the velocity of the charged particles. ANSYS Maxwell natively solves for the electric field, both vector and magnitude, in these simulations. That electric field can then be used to approximate the electron and hole velocities at any position within germanium [9]:

$$\vec{v}_{drift}(\vec{x}) = \frac{\mu_0 \epsilon(\vec{x})}{\left[1 + \left({}^{\epsilon(\vec{x})}/_{\epsilon_0}\right)^{\beta}\right]^{1/\beta}} \qquad \text{(Eq. 1)}$$

where v_{drift} is the velocity vector, μ_0 is the mobility, ϵ is the electric field at any point $\vec{x}$, and ϵ_0 and β are both constants. $\epsilon_0 = 210.5\ {}^{V}/_{cm}$ and $\beta = 1.36$ for holes and $\epsilon_0 = 275\ {}^{V}/_{cm}$ and $\beta = 1.32$ for electrons.

3.3. Electron Transport Modeling

The electric fields and charged particle velocity calculated by ANSYS Maxwell can be used to determine the path a charged particle will take from the point of gamma-ray interaction until it is collected by the GeGI electrode. As it moves on this path it induces current on all other GeGI electrodes. Determining the modeled correlation between starting position and induced current, one can use experimentally measured induced current to determine the gamma-ray interaction location and improve near-field imaging capability with the GeGI detector.

The path a charged particle takes within the germanium is calculated from the electron and hole velocity vectors obtained by the ANSYS Maxwell R18.2 simulation. Those particles are then transported along the electric field lines, based on the velocity map generated in Maxwell, until they terminate at the electrodes. The transport is done with gradient time steps, larger in the middle of the detector and then progressively finer as the particles near the electrode, and at each time step the current on the primary and

neighbor electrodes is calculated using the Shockley-Ramo Theorem. The simulation does not include any of the photon transport mechanisms nor does it include the photon interactions that would generate the electron-hole pairs.

3.3.1. The GeGI Model

The GeGI was first modeled in three-dimensions, Figure 2a, however the computational power required to solve this simulation proved excessive. Thus, the GeGI was reduced to a two-dimension slice from the center of the detector, and symmetry was used to only model half of the full detector's width. The two-dimensional model is of a 10 mm thick section of germanium, on the top and bottom are 1 mm thick aluminum electrodes. The strip pitch is 5 mm and there is a 0.25 mm gap between strips. A zoomed in view of the strip gap is shown in Figure 2b, which also shows the meshing structure used in the solution of the electric field. At the edge of the germanium is a guard ring. The top electrodes are set to 1 kV, the bottom electrode is set to ground, and the guard ring is also set to ground. The left edge of the model, which physically represents the middle of the germanium crystal, has a symmetric boundary condition, while the right edge has no defined boundary condition.

The model had 8 electrodes, which would result in eight unique weighting fields determined by which electrode collected the charged particle. To improve computational speed, the mesh under the collecting electrode was approximately 50 times finer than through the rest of the germanium.

a) 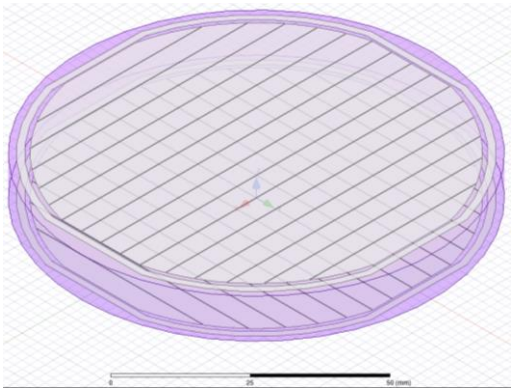 b) 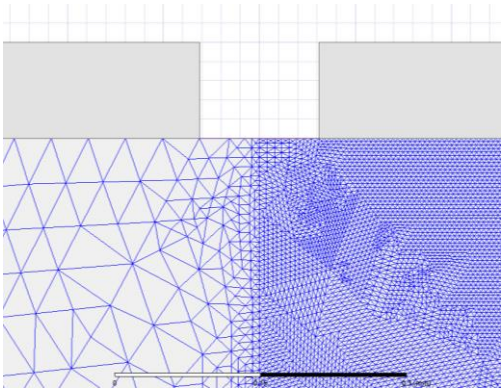

Figure 2. a) A transparent view showing the orthogonal strips on the pack of the germanium. b) Comparing the difference in mesh size between the collecting strip and the bulk germanium.

Based on the boundary conditions, ANSYS Maxwell R18.2 calculated the electric field vector at every mesh point. This was then used to determine the electron and hole velocity vectors at each mesh point. The velocity vectors were exported from ANSYS Maxwell R18.2 at half a million discrete locations along a uniform grid within the germanium. Linear interpolation was used to determine the velocity between the discrete locations.

3.3.2. Charged Particle Transport Code

The data from the ANSYS Maxwell simulations; the electric field, the eight unique weighting fields, and the particle velocity; were used by a custom charged particle transport code to calculate the induced currents as a function of the charged particles movement through the germanium crystal. The starting position of the charged

particles, the spatial distribution of the starting charged particles, whether the particles are holes or electrons, and the number of particles generated were user inputs to allow different calculations.

The starting position of the charged particles was set to one of two options. The first creates every particle at the exact same location and the second option creates a uniform distribution of specified width. This width can either be the entirety of a strip to see the total strip response, or it can be smaller to match experimental data with a collimated photon beam. The random starting positions were set by Python 2.7's NumPy package without predefining a seed. The charge of the particle was either negative or positive to specify the difference between electrons and holes. The number of particles specified was linearly proportional to the energy deposited in the crystal.

After the particles are created, they are transported until they terminate at an electrode. The time step used during the transportation is non-uniform, as the particle nears the edge of the crystal the time step reduces. This reduction in time step helps more finely track the movement as the particle nears the electrode as this is the most critical region when calculating the induced current.

At every time step the induced current on the electrodes were calculated. Although the induced current can be calculated for every electrode, the raw GeGI data only reports from the four closest neighboring electrodes for each event. To match the physical data, the simulation only calculated induced current for the four closest neighbor strips. The final output for each charged particle transported was the starting

and ending location, the time it took for the particle to travel, the charge collected by the primary strip, and the nearest and second-nearest neighbor charges.

3.3.3. Dimensionless Number

As charge moves towards the electrode, it will induce a current on neighboring strips. Comparing the induced current to the left and the right of the primary strip there is a connection between the location of the charge particle creation and the relative current to the left and right of the primary strip. To quantify this, a dimensionless number was defined, ψ that ratios the difference in induced current on either side of the primary strip to the induced current on the primary strip. The value of this dimensionless number is dependent upon its uniqueness as a function of the gamma-ray interaction location.

$$\psi = \frac{\left(I_{right,1} + I_{right,2}\right) - \left(I_{left,1} + I_{left,2}\right)}{I_{primary}} \qquad \text{(Eq. 3)}$$

3.3.4. Experimental Validation

A data set collected for a previous publication, [1], was reanalyzed to determine if ψ was merely a relic of the simulation. The experimental procedure will not be reproduced in full, but in summary, a collimated beam of ^{154}Eu photons was measured at thirty horizontal and thirteen vertical locations across the GeGI's face. Between each measurement the photon beam was displaced by 1/12th of the strip pitch, 0.42 mm.

The GeGI's raw data reports the energy deposited on the primary collecting strip as well as the energy induced on the first and second neighboring strips for each event.

While technically, energy is not induced on the neighbor strips the GeGI converts the current on the strips into the equivalent energy deposition had this current been from a photon interaction.

3.4. Simulation Results

Presented in this section are the results of the two simulations, first the ANSYS Maxwell R18.2 simulation of the electric and weighting fields within the germanium, and second the use of that simulation to transport charged particles. Interpretation of the transport simulation is done through the creation of a new dimensionless number that allows comparison of the simulations to experimentally collected data.

3.4.1. Electric Field Calculation

The electric field within the germanium is uniform except at two locations, near the guard ring and the gaps between electrodes. The guard ring is grounded whereas the electrodes are at 1000 V, this difference in voltage results in a sharp gradient of the electric field, Figure 3. This gradient extends under the edge-most electrode resulting in the edge-most electrode being the only one with a non-symmetric electric field; this will cause differences in the charged particle transport under this edge-most electrode compared to any other electrode. Although these differences have not been simulated in depth their impact has been seen in experimental data, Figure 1. As the edge-most electrode only has neighbors on a single side, the method of localization prevents any

events occurring under this strip from being localized and thus it is not used as a starting point for any simulated charged particle.

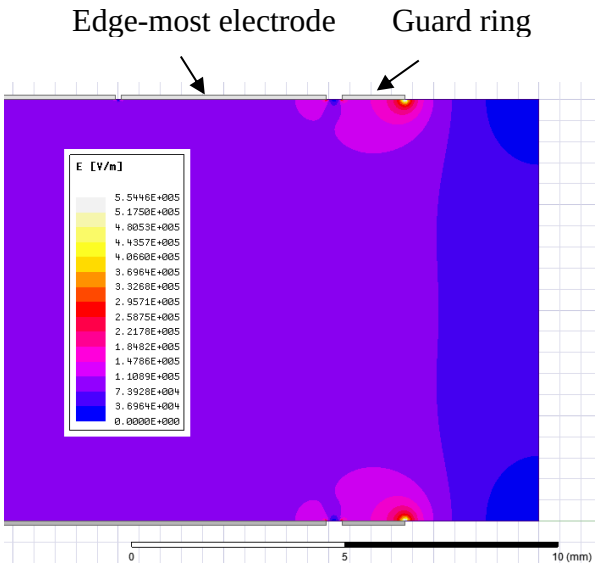

Figure 3. Electric field magnitude at the edge of the germanium.

Focusing on strips in the center of the detector, the electric field lines, Figure 4, show that each strip is isolated and that events are collected by the strip under which they originate. When charged particles originate within the gap between two strips, they are drawn to the nearest strip. These gap regions have the lowest electric field, Figure 5, causing charged particles within the gaps to move more slowly towards the strips. The full effect of these gap events will be discussed later in this paper.

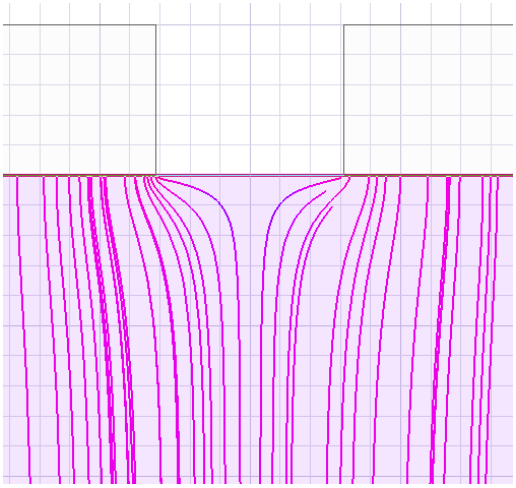

Figure 4. Electric field lines drawn in a gap region of the germanium.

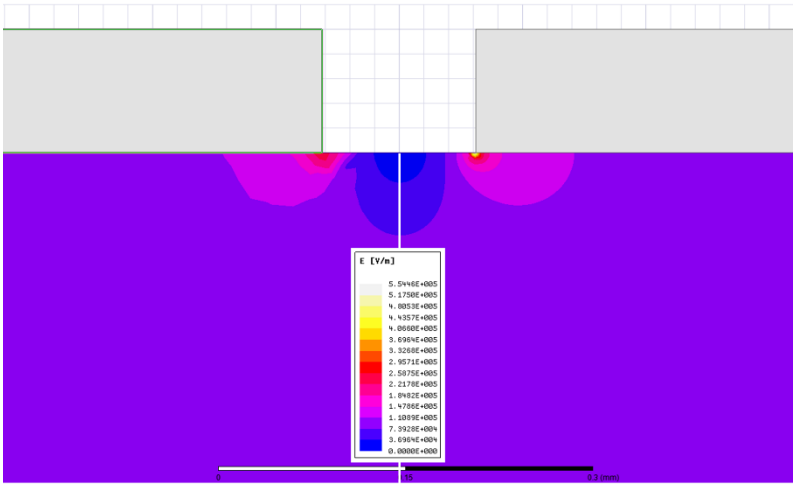

Figure 5. The boundary between the "primary" strip and the bulk demonstrates the difference made by the increased mesh density.

3.4.2. Validating Charged Particle Transport Code

As the charged particle transport code was written specifically for this research, the validity of its results was tested. A test of the charged particle transport simulation started particles uniformly across a single strip and recorded their ending position. As

the majority of the electric field lines traveled orthogonally between the electrodes on the top and bottom of the GeGI, the code should show that the ending positions match the starting position. The only electric field lines that curve were the lines that existed within the gaps between electrodes, therefore all events created in the gaps should be collected on the edge of the electrode. As shown in Figure 6a, the events are drawn from a uniform distribution covering the full strip width, and half of the gap width on either side of the strip. Figure 6b shows the histogram of where the charged particles terminated. The collection is uniform and matches the starting location distribution in the center of the electrode. At the edges there is significant peaking as all events created within the gaps follow the electric field lines to termination at the edge of the electrode.

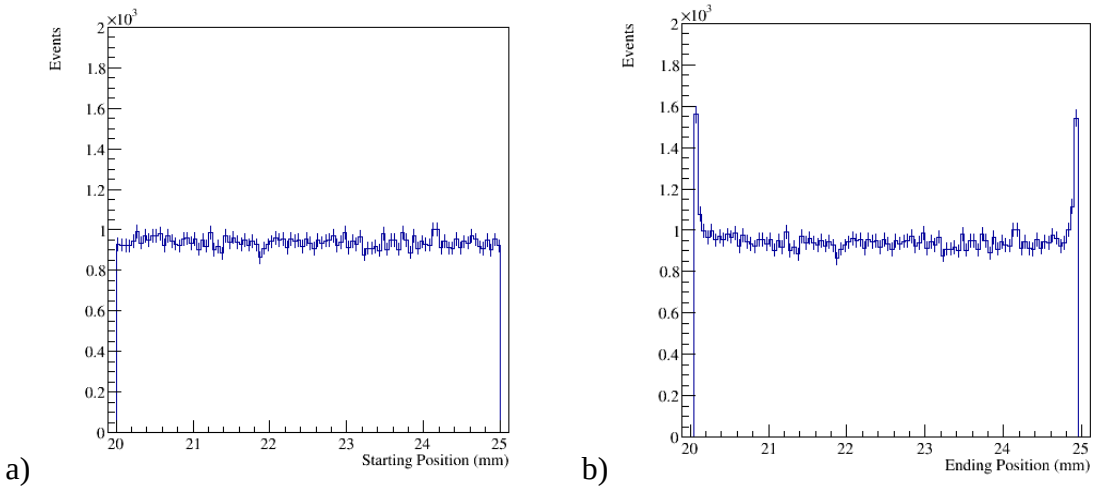

Figure 6. The starting and ending positions of the simulation.

3.4.3. Primary Current

The energy a gamma-ray deposits within a germanium detector is measured by the number of electron-hole pairs created and thus the current on the primary strips, one

primary strip on the top of the germanium and one primary strip on the bottom. Although the majority of the current comes from the charged particles being collected by the primary electrodes, their movement will also induce current on every strip. This induced current was calculated by the Shockley-Ramo theorem at every time step and then integrated over the full lifetime of the charged particle to determine the total induced current.

A histogram of the induced current, solely due to the charge movement, on the primary strip is shown in Figure 7. The green filled portion represents the events that are in the gap between strips and accounts for 4.5% of all events. Plotting the total induced current as a function of event starting location results in Figure 8. The events that are created in the gaps induce more current and the minimum induced current is in the center of the strip. The induced current is a function of the particles' velocities as they moved towards the electrode. The corners of the electrodes have an electric field approximately five times greater than the germanium average and thus charged particles that start in the gaps are accelerated by this higher electric field which results in a larger induced current. It also shows a symmetry that the reduction in current is the same to the left or the right of the primary strip, this was expected as the electric field had left-right symmetry.

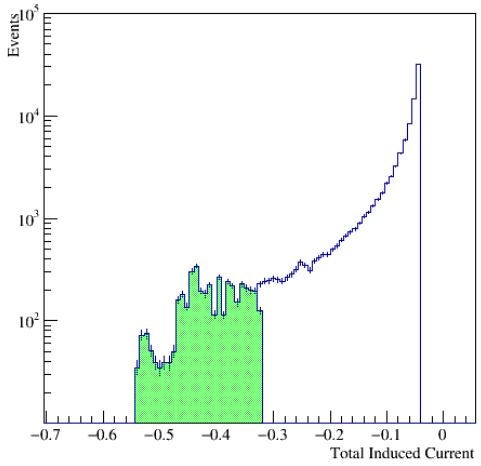

Figure 7. A histogram of current on the primary strip. The green shaded area are events that are created within the gaps between electrodes and contain 4.49% of all events.

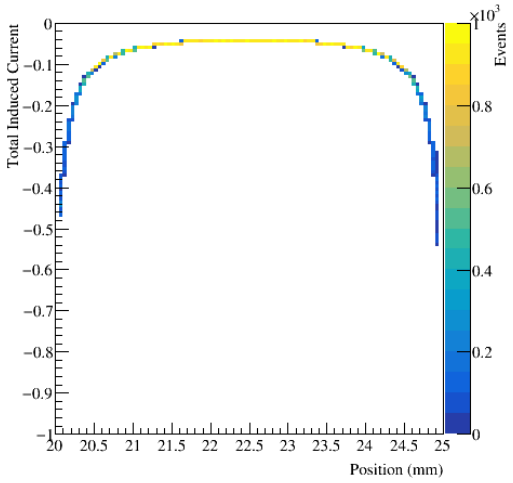

Figure 8. A histogram of total induced current on the primary strip as a function of the starting location of the event.

3.4.4. Neighboring Current

As the induced current was calculated for the primary strip, it was also calculated for its left and right neighboring strips. Current was induced on every strip within the detector, but the magnitude of the current was strongly attenuated by distance from the moving charge under the primary electrode. From the GeGI detector, the induced current could be obtained for the nearest two neighboring electrode strips. Therefore, only these four neighbor-induced currents were calculated as they could be directly compared to experimental data.

The four neighbor currents are plotted in Figure 9. The left column, labeled “left” and “right”, are the nearest neighboring strips, and the right column, named “left 2” and “right 2”, are the second nearest neighbors. The shape of the current histograms for the direct neighbors match that of the primary current, although the sign is flipped. Again, the green filled histogram demonstrates the response from events that occur within the gaps. The neighbor currents are on the same order of magnitude as the primary strip; however the second neighbor are 100 times weaker.

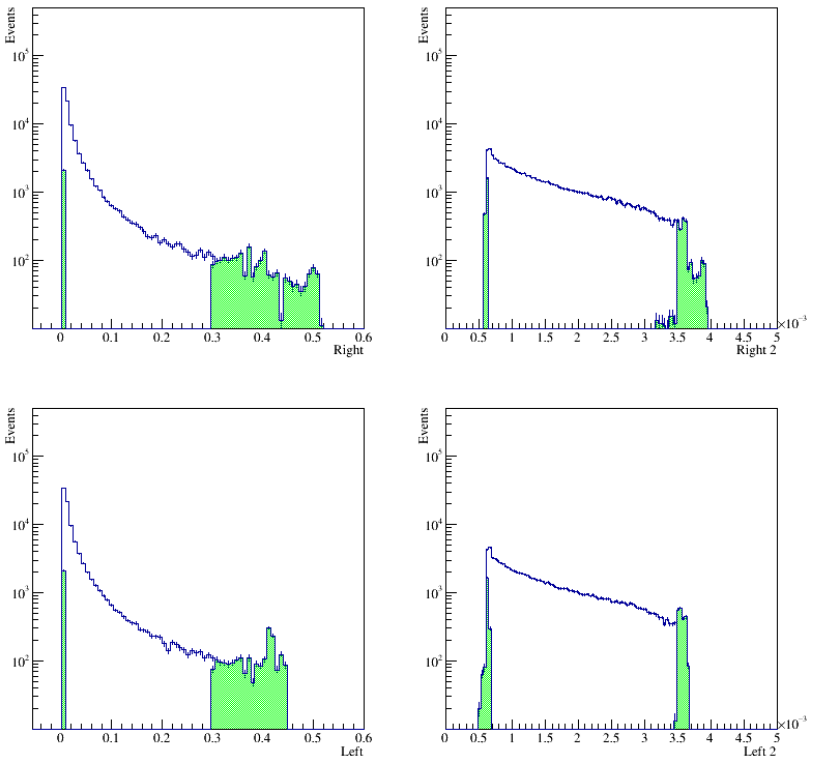

Figure 9. Comparing the neighbor and second neighbor's current distribution, on the top is the right first and second neighbor and the bottom is the left first and second neighbor. The green shaded area are events that are created within the gaps between electrodes and contain 4.49% of all events.

When the difference of the left-right neighbor histograms, on an event-by-event basis, are taken the result is a winged histogram, Figure 10. The majority of the time the values of the left and right neighbors are similar, hence a difference of zero. What stands out are the gap features. These exist in the difference histogram, which implies that a high current on the left neighbor results in a current of almost zero on the right neighbor.

This indicates that the values of these neighbor currents may be related to the position of the initial event.

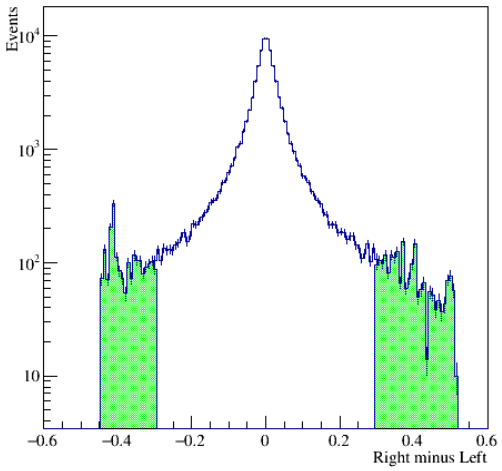

Figure 10. The distribution of the difference between Right and Left induced current. The green shaded area are events that are created within the gaps between electrodes and contain 4.49% of all events.

That same data set, plotted now as a function of event ending position in Figure 11, shows that the difference in left and right neighbors is dependent on the events location and varies almost linearly in the center of the strip, but very nonlinearly for events within the gaps. The linearity implies that, in the center of the strip, the difference in neighbor induced current may be helpful to determine the sub-strip position of photon interaction. However, the non-linearity for gap events, stemming from the large gap induced current, will need to be carefully accounted for.

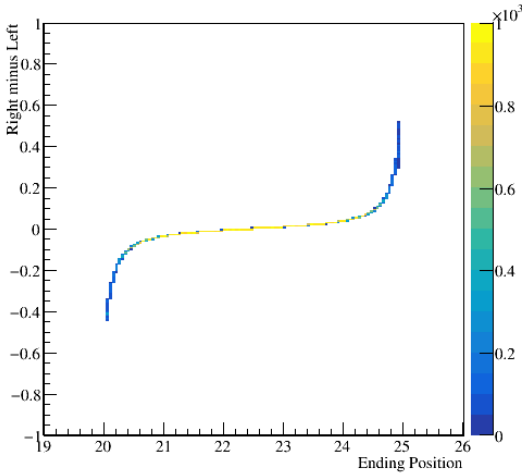

Figure 11. The difference in right neighbor and left neighbor current as a function of event ending position.

3.4.5. The ψ Dimensionless Number

This dimensionless number, ψ, is only calculated from the closest two strips to the left and right of the primary collecting strip because the induced current is reduced with distance from the initiating event. Events that happen near the edge of the detector are unusable because they have only one or zero strips neighboring a side. While a concern, this is less important as the edge most strips of the GeGI have the lowest intrinsic efficiency [1], approximately 30% of the efficiency as the center of the detector. Measurements relying on those strips to determine sample activity would take three times as long, which goes against the paradigm of the GeGI being used to triage samples.

Calculating the ψ value for a uniform distribution of events that span across a single electrode, Figure 12, shows that the ψ value is naturally bounded between [-1, 1].

The center of the distribution is curved, but the peaking at the edges are strongly impacted by events occurring within the gap between electrodes.

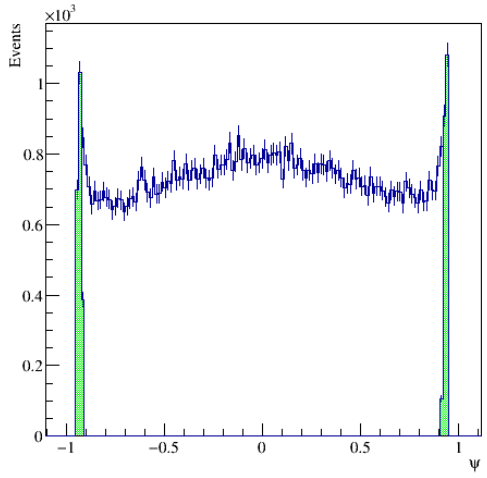

Figure 12. The ψ distribution from a source uniformly across an entire strip. The green filled regions are the events that started within the gap between electrodes.

3.4.6. Testing ψ

Figure 13 shows that for any given position across a strip, there is a single ψ value. This linearity allows the solution to the inverse problem, if the ψ is known for an event its relative lateral position under a strip can be directly calculated. A linear fit to the ψ as a function of event starting location well represents the data with $R^2 = 0.993$. The slope is consistent among the different strips, excluding of course the edge-most strips, and it is only the constant that needs to be changed to account for the different strips.

$$\psi = 0.377x - 8.48 \qquad \text{(Eq. 4)}$$

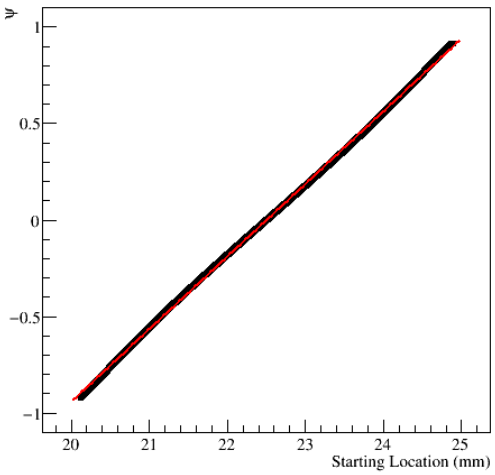

Figure 13. A uniform distribution of events over the full strip demonstrates both the uniqueness and linearity of ψ. The red line is a linear fit with $R^2 = 0.993$.

3.4.6.1. When ψ Fails

The dimensionless number ψ is linear for events that terminate on the electrode; however, there are simulated cases when events created within the gap do not reach the electrode and thus calculate a ψ value that is unrelated to the event's position. These events are terminated before they reach the electrode because they leave the germanium volume and enter the vacuum region, a feat that physically cannot happen. This is a failure of the simulation and would not be seen in experimental data. Plotting ψ as a function of starting position show these failed events in red circles, Figure 14a. These events are isolated by only plotting events which have their ending position within the gaps, Figure 14b. What is interesting is that the events that are in the gap on the right side of the strip predominantly has a low ψ value. By looking at the ψ one would assume that the event happened on the left side of the strip. This would result in a

minimum error of 5 mm. In 749,683 simulated events only 317 ended within the gaps, a failure rate of 0.04%, meaning that the statistical value of the rest of the data set, when these failed cases are removed, is still valid.

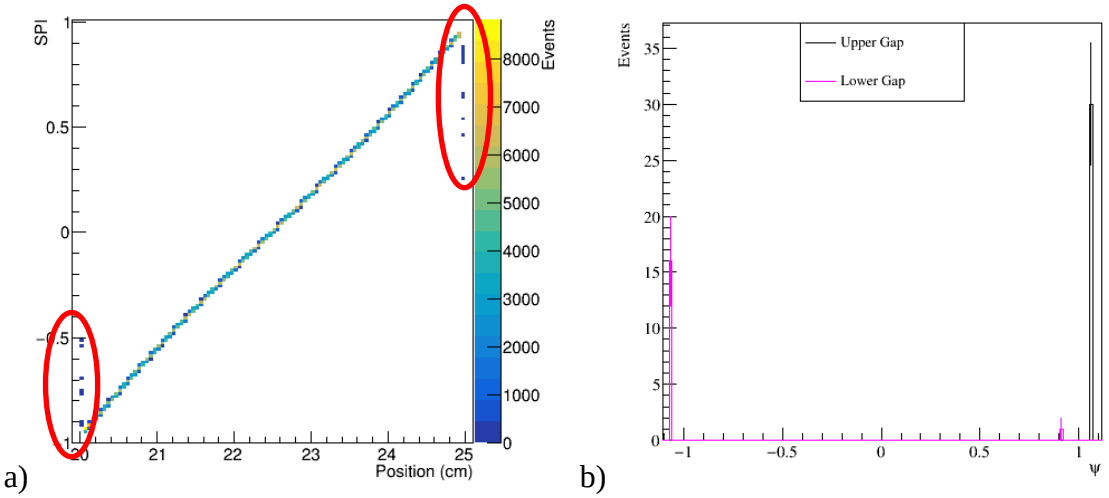

Figure 14. The events in the gaps do not have any seeming correlation with the ψ value

3.4.6.2. Comparison to GeGI

Figure 15 shows the calculated difference between rightward and leftward neighboring strip responses from an experimentally collected data set It has the same shape as Figure 10 with a sharp peak and "humps" that are indicative of events occurring within the gaps between strips. The distribution is non-symmetric because this measurement was not taken at the center of the strip. The magnitude between the experimentally collected data and simulated data are different, as they are reported in different units. The GeGI reports the energy on the neighboring strips, whereas the

simulation deals in the total induced current. This difference in magnitude is not crucial because what matters is that the shape of the distribution was similar.

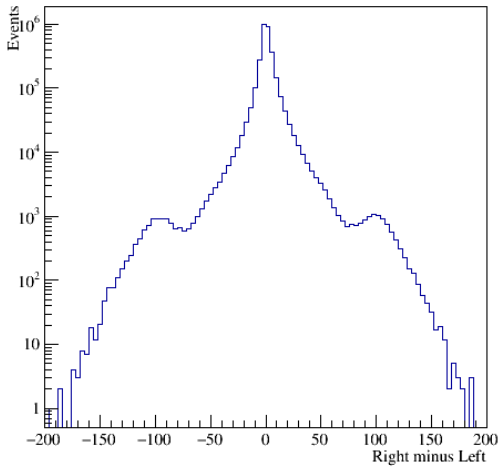

Figure 15. The difference between the right and left strips within the GeGI.

The ψ value was then calculated from each of 30 measurements made with a collimated photon beam that was rastered across two and a half strips, the data is shown in Figure 16. In this figure it is shown that the ψ value maps to the sub-strip position of the collimator and therefore the ψ value is indicative of where the photon interaction is occurring. It is therefore possible to solve the inverse problem of calculating the ψ value and then determining the location of the event.

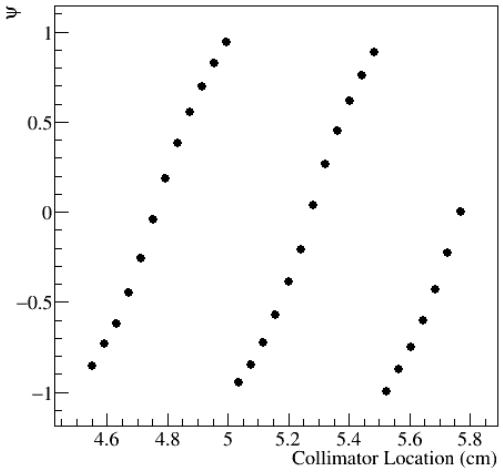

Figure 16. A plot of ψ calculated from experimental data covering measurements crossing two and a half electrodes.

This is an improvement over what the GeGI software natively provides for sub-strip event locations. Figure 17 shows a comparison of the ψ method with the GeGI method. The GeGI's method can only calculate five positions per strip and the calculated position does not increase linearly or evenly as would be expected from the measurements. Comparing the ψ method and the GeGI method to determine the position of interaction to the known true value, the ψ method is an improvement of up to 20%.

The calculation of ψ is a simple equation to add to a post-processing data script that will result in a more accurate measurement of an isotope's location. This improvement in locational accuracy feeds into the spatially dependent efficiency and results in a further increase to the accuracy of measuring a sample's activity.

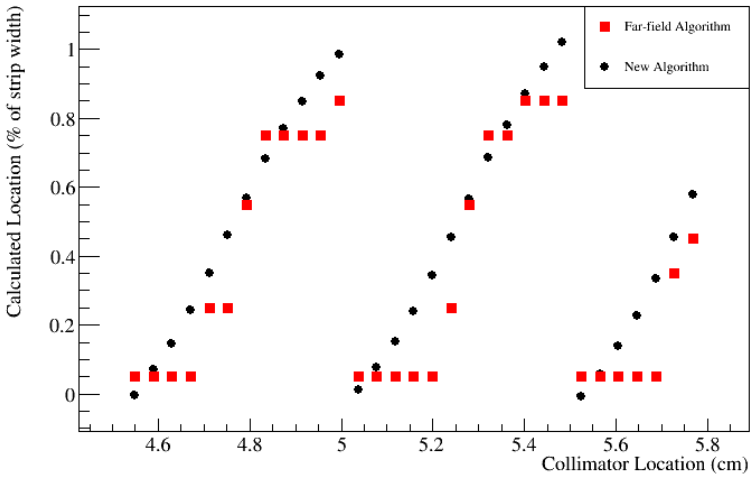

Figure 17. A comparison of using $\boldsymbol{\psi}$ to calculate position, black circles, to the GeGI's native attempt, red squares.

3.5. Conclusions

The GeGI DSSD was modeled using ANSYS Maxwell R18.2 to calculate the electric fields within the germanium crystal and to calculate the electron and hole velocity profiles. From this data set, a particle transport code was written to track the electrons and holes as they move through germanium and calculate the current induced on electrodes by the moving charges. The simulated current induced on the neighbor strips was validated by experimental results. It was also found that simulated events originating in the gaps between electrodes induce significantly more current than events that are directly under an electrode. This is due to the lower electric field experienced within the gap and the longer lifetime of the charge before it is collected on an electrode. These gap events are excluded from data analysis because in a real detector they would not be collected within the trigger window.

Having created a model that can match experimental data, a dimensionless number was derived that can determine the neighbor-induced current to calculate the lateral position under a strip. The dimensionless number, ψ, is linear as a function of position so that it can be used inversely to calculate the position of the event as a function of induced currents on the neighboring strips. When starting events were modeled to match a beam of photons rather than a uniform illumination, the ψ distribution showed the beam location and could be used to determine the width of the beam.

The dimensionless number ψ is a better method of determining the sub-strip positioning of an event than is natively used by the GeGI software and will allow greater precision of event localization. Knowing the location better will feed into the spatially dependent intrinsic efficiency of the GeGI which will ultimately reduce the uncertainty of source quantification.

3.6. References

1. T. W. Jacomb-Hood, J. E. Fast and M. M. Craig, "Characterization of the spatially dependent intrinsic efficiency for a germanium double sided strip detector," Spectrum, p. In Submission, 2020.
2. E. Hull and M. Kiser, "Radioactive Threat Vision via Quantitative Gamma-ray Imaging," in NCT CBRNe USA, Washington DC, 2016.
3. ANSYS Maxwell, "ANSYS Maxwell Users Manual v18.2," 2017.

4. J. Jin, The Finite Element Method in Electromagnetics, 2nd. ed., New York, NY, USA.: John Wiley and Sons, Inc., 2002.
5. D. Kincaid and W. Cheney, Numerical Analysis Mathematics of Scientific Computing, American Mathematical Society, 2002.
6. W. Shockley, "Currents to conductors induced by a moving point charge," Journal of Applied Physics, vol. 9, no. 10, pp. 635-636, 1938.
7. S. Ramo, "Currents Induced by Electron Motion," Proceedings of the IRE, pp. 584-585, 1939.
8. T. W. Raudorf and R. H. Pehl, "Effect of Charge Carrier Trapping on Germanium Coaxial Detector Line-Shapes," Nuclear Instruments & Methods in Physics Research Section a-Accelerators, Spectrometers, Detectors, and Associated Equipment, vol. 255, no. 3, pp. 538-551, 1987.

4. CONCLUSIONS

Three types of measurements are made on a nuclear forensic sample: radiation counting, imaging and microscopy, and isotope mass spectroscopy. A variety of different measurement techniques are used within each broad type of measurement, and these are determined to best measure each unique sample. Any collected sample that is radioactive will have gamma-ray spectroscopy used as a first measurement for bulk analysis. The results of the gamma-ray spectroscopy can be used to inform which techniques will be used to further analyze the sample. This process could be significantly improved if a single in-field nondestructive measurement were to provide an isotopically sensitive spatial distribution of the radionuclides present and isolate the subset of the sample that is most important to analyze.

The fact that the efficiency of the detector changes on the pixel level was expected from literature, but the fact that the efficiency changes across multiple electrode strips, and changes significantly, was unexpected. In regions where electric field uniformity is expected there was up to a 20% reduction in efficiency. This reduction based on position is separate from the reduction in efficiency as a function of the photon's energy.

It has been shown that the absolute efficiency as a function of space is related to the bulk efficiency of the detector. Thus, a single bulk efficiency measurement in the field can be used to calibrate the detector for both its energy dependent and spatially dependent efficiency.

The spatially dependent efficiency proves an enhancement over the current strategy of calculating the efficiency based on a volume average. When calculating a samples activity this will result in an improvement by approximately 6—20% depending on the size of the sample and where on the face of the detector it is being measured.

The experimental results seen with the GeGI DSSD were validated by modeling the detector using ANSYS Maxwell R18.2. The simulated movement of the electrons within the crystal, and the current thereby induced, matched the experimental results and was used to derive a dimensionless number to better calculate the lateral position under a strip that the gamma-ray interaction occurred. The dimensionless number, ψ, was linear and unique as a function of position so that it can be used inversely to calculate the position of the event as a function of induced currents on the neighboring strips.

The dimensionless number ψ is a better method of determining the sub-strip positioning of an event than is natively used by the GeGI software by up to 20%. This improvement in event localization feeds into the spatially dependent efficiency and results in an improved triage of nuclear forensic samples.